Discovery of cloud top ozone on Venus

Emmanuel Marcq, Lucio Baggio, Franck Lefèvre, Aurélien Stolzenbach, Franck Montmessin, Denis Belyaev, Oleg Korablev, Jean-Loup Bertaux

Discovery of cloud top ozone on Venus

Emmanuel Marcq[a,*], Lucio Baggio[a], Franck Lefèvre[a], Aurélien Stolzenbach[a], Franck Montmessin[a], Denis Belyaev[b], Oleg Korablev[b], Jean-Loup Bertaux[a,b]

[a] *LATMOS/CNRS/Sorbonne Université/UVSQ, 11 boulevard d'Alembert, F-78280 Guyancourt, France*
[b] *Space Research Institute (IKI), Russian Academy of Sciences, Moscow 117997, Russia*

Abstract

After the first sporadic detections of an ozone (O_3) nighttime layer in the 90-100 km altitude range (Montmessin *et al.*, 2011), we report here the discovery of another, permanent ozone layer on Venus, restricted to high latitudes (polewards of 50° both N and S) and located at the upper cloud level near 70 km. This detection was performed during a reanalysis of the whole SPICAV-UV nadir dataset through UV absorption near 250 nm in the backscattered solar light. The O_3 volume mixing ratio peaks in the 10 to 20 ppbv range, yielding observable column densities in the 0.1 to 0.5 Dobson units (DU), comparable to nominal values on Mars but much smaller than for Earth ($\sim$ 300 DU). These measurements are supported by our 3D-photochemical model coupled with the LMD-IPSL GCM (Lebonnois *et al.*, 2010), which indicates that the ozone layer identified by SPICAV results from downward transport of O_2 ($\sim$ 50 ppmv) molecules over the poles by the mean meridional circulation. Our findings do not contradict previous upper limits ($<$ 2 ppmv) based on O_2 measurements (Mills, 1999), since they were

*E-mail: emmanuel.marcq@latmos.ipsl.fr

restricted to lower latitudes only.

Keywords:

Venus, atmosphere, Ultraviolet, observations, Atmospheres, composition

1. Introduction

Ozone (O_3) has been observed in the ultraviolet (UV) domain in all three telluric atmospheres of the inner solar system: on Earth, discovered in the early 20th century; on Mars, by Barth *et al.* (1973) in the early 1970s from *Mariner 9*; and more recently on Venus using the SPICAV-UV spectrometer on board *Venus Express* in stellar occultation mode (Montmessin *et al.*, 2011). Unlike Earth and Mars, this Venusian ozone layer appears to be sporadic and located at very high altitudes (circa 10^{-2} mbar for Venus instead of 1-50 mbar for Earth and Mars), so that it is the thinnest of all in terms of local number densities. Here we report the discovery of permanent, denser ozone polar caps located at high latitudes near cloud top level, where pressure is similar to ozone-bearing layers in the atmospheres of Mars and Earth.

This discovery happened during our reanalysis of the whole SPICAV-UV nadir dataset after the end of *Venus Express* in 2014. Although 1D photochemical models did not predict any significant O_3 near cloud top (Yung and Demore, 1982; Krasnopolsky, 2013), we observed in our first processing of SPICAV-UV nadir data (Marcq *et al.*, 2011, Fig. 12) that another absorption occurred sometimes near 250 nm, and suggested that it might be caused by ozone.

Aside from the primary goal of our reanalysis (namely, investigating the climatology of cloud top SO_2 in the 2006-2014 timeframe) that will be dis-

cussed in subsequent papers, we included a possible ozone absorption in our study and found numerous robust detections at high latitudes that are detailed hereafter. The observational data set and the pre-processing into spectral radiance factors are described in Sec. 2, our forward radiative model is detailed in Sec. 3, and our results are discussed, compared with previous upper limits, and interpreted using a 3D photochemical model in Sec. 4.

2. Observations

2.1. Overview

The SPICAV-UV spectrometer (Bertaux *et al.*, 2007) on board *Venus Express* covered the 118-320 nm spectral range, sampled at 0.55 nm with a Field of View $1° \times 3.16°$. Our studies have used 5 lines of the CCD (from line #141 to #145) corresponding to the region where the spectrometer slit is narrow and the spectral resolution higher (1 nm). Integration time was 0.64 s. Although SPICAV-UV can be used also in limb or occultation modes, we only focus here on day side near nadir observations (whenever the line of sight intersects the solid planet), therefore observing the sunlight backscattered by the upper clouds of Venus.

2.1.1. Coverage

The spatial coverage of these 1508 near nadir observations acquired between orbits #0041 (2006-06-01) and #3146 (2014-11-20) is shown on Fig. 1. We can see that very few observations were acquired southwards of 80°S compared to northwards of 80°N. This is due to the quasi-polar and highly elliptical orbit of *Venus Express* (pericenter near 78°N). Also, the coverage in

Figure 1: *Left*: areal coverage of near nadir SPICAV-UV observations with respect to latitude for north and south hemispheres. *Right*: areal coverage of near nadir SPICAV-UV observations with respect to local solar time for both hemispheres.

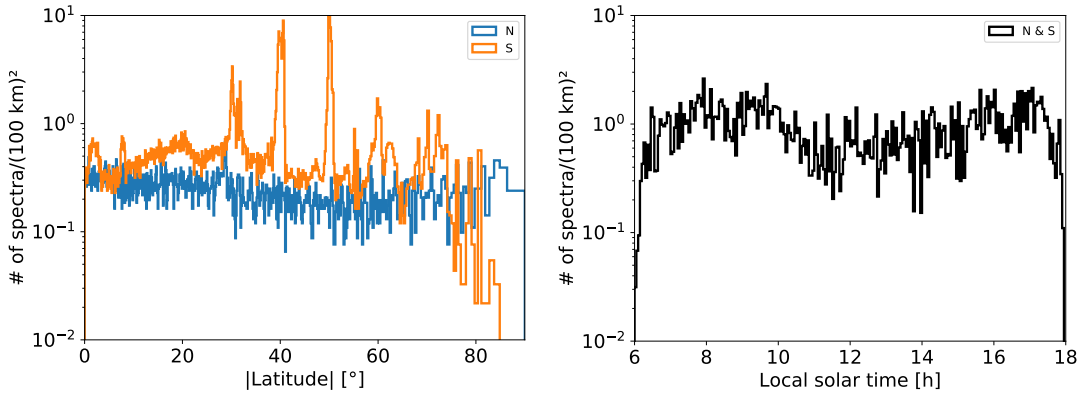

the southern hemisphere is less uniform than in the northern one, since most southern observations were done in *pointing* mode, where SPICAV FOV was fixed relative to the Venusian surface. In contrast, most northern observations were done in *latitudinal scan* mode, sweeping a large latitudinal swath under the spacecraft orbit with a constant (and small) emission angle. Coverage in local time is more regular, with a small decrease near local noon due to spacecraft constraints on the phase angle (direct illumination of the spacecraft radiator was limited to short amounts of time).

2.2. Instrumental correction

The first steps of the processing have changed little compared to those described in Marcq *et al.* (2011). First, non-uniform dark current templates (acquired with light intensifier switched off) are rescaled in order to match the

operational parameters (notably, the temperature) at the time of the science mode operation. These dark frames are subtracted from the light-exposed frames. Cosmic hits are removed, as well as a pseudo-periodic electronic readout artifact. Flat-field corrections are also implemented. Based on the rich spectral structure of the solar spectrum in the 200-315 nm range as can be seen in Marcq *et al.* (2011, their Fig. 1), sub-pixel wavelength assignment could be performed for each acquisition (there is a typical drift of 1-2 pixels (0.54-1.08 nm) during a 30 min long observation sequence).

External solar stray light is not a problem for near-nadir observations, since the phase angle is always smaller than 90° so that Venus backscattering is always dominant. Internally, one significant source of contamination comes from the blurring due to the point spread function (PSF) of the instrument. Its shape is empirically modeled as a two dimensional Gaussian core with a radius of a few pixels, summed to an extended halo, which decrease asymptotically as a power function. The parameters of this model have been preliminary estimated by exploiting a few technical observations. In order to reduce the far wing impact of the PSF and tentatively access the native spectral resolution of the instrument, an inversion is performed using an iterative accelerated damped Richardson-Lucy algorithm (White, 1994; Biggs and Andrews, 1997). This step greatly reduces spectral distortions due to spectral blur (Fig. 2). Also, it accounts for and subtracts the cross-contamination of spatially separated CCD lines. This happens for instance when faint spectra are acquired in the narrow segment of the slit while the wide segment is fully illuminated.

Figure 2: *Left*: Observed spectrum before (L1A) and after (L1B) Richardson-Lucy deconvolution, compared to our reference solar spectrum at SPICAV resolution. Note that the deconvolution (i) restores the full instrumental resolution of the solar features; and (ii) effectively removes contamination due to the extended halo of the PSF at shorter wavelengths.

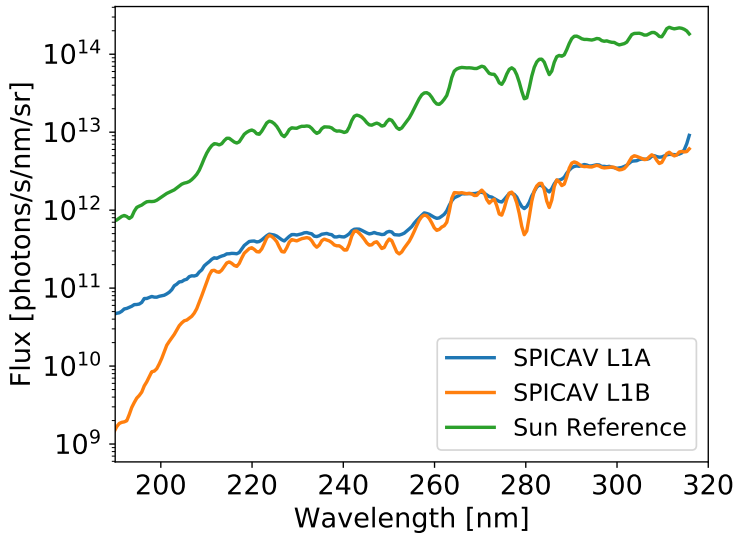

2.3. Spectral radiance calibration

In order to get an absolute photometric calibration for the spectral radiance $B(\lambda)$, we have preliminarily observed a few selected UV-bright stars, for which a reference spectra existed in the CALSPEC database (Bohlin *et al.*, 2014). From these observations, an effective area can be defined for each wavelength as the ratio between the number of detected photons per unit of time and the incoming stellar flux. This effective area is of course a function of the wavelength, but also a function of the age of the instrument. The actual calibration step consists in multiplying the nadir spectra by a calibration vector which takes into account the amplifier gain, the effective area and the angular field of view of each pixel. These studies suggest that for the low gain values used in these near-nadir observations, no significant aging trend should be expected over the duration of the mission.

2.4. Radiance factor calibration

Following our previous work (Marcq *et al.*, 2011, 2013), we define the *radiance factor* $\beta(\lambda)$ through the expression $\beta(\lambda) = \frac{I(\lambda) \times \pi \text{ sr}}{F_\odot(\lambda)}$ where $I(\lambda)$ is the received spectral intensity and $F_\odot(\lambda)$ is a reference top-of-atmosphere solar spectral irradiance as received by Venus. $\beta(\lambda)$ differs from the spectral albedo by not depending on the solar zenith angle value, and thus can be meaningfully defined even on the night side near the terminator – solar zenith angle (SZA) a few degrees larger than 90°, where some scattered solar light can be still detected. Although our pseudo-spherical radiative forward model can account for such a geometry, we restrict our analysis to SZA $< 88°$, so that we can still consider the Sun as a point-like source (i.e. considering the same airmass over the whole extent of the solar disk). Since the angular

diameter of the Sun as seen from Venus is a mere 0.8°, this approximation results in a relative error smaller than 0.5% on our synthetic radiance factors, according to our numerical testings.

For the scope of this work, our reference spectra are the 30 days running averages of the daily solar irradiance from the SOLSTICE II database (McClintock *et al.*, 2005). The actual data in the MUV range have been slightly corrected in order to fall back to a previous calibration, as the more recent one has a feature around 230-240 nm for which no good agreement can be found in the models, whichever the set of chosen parameters.

The ratio between observed spectral radiances and the solar spectral irradiance is very sensitive to precise spectral alignment and matching spectral resolution, due to the numerous solar lines. This results in "wiggles" on a wavelength scale of the apparent line width (1-2 nm). It is reasonable to assume that the expected radiance factor is smooth on this scale. We therefore applied a regularizing procedure consisting in: (a) determining the relative alignment of the spectra at the level of 0.05 nm; (b) locally adjusting the spectral resolution for each line; (c) performing a sensitivity analysis and retaining only a few dozen wavelength positions (typically the two inflection points for each of the solar spectral lines) with vanishing dependence on the resolution parameter; (d) interpolating between the fixed points with a smooth function.

3. Forward Model

The core of our forward model is the publicly available SPSDISORT v2.0 generic radiative transfer code. SPSDISORT is the pseudo-spherical ver-

sion of the well-known DISORT code (Stamnes *et al.*, 1988; Dahlback and Stamnes, 1991).

3.1. Vertical profiles

Our model atmosphere is divided into 30, 2-km thick homogeneous layers extending from $z = 50$ km ($P = 1037$ mbar) up to 110 km. The albedo of the virtual surface at the bottom of our model is set to 0.33, but we checked that the model does not exhibit any sensitivity to this bottom albedo, since the overlying atmosphere is optically thick (and absorbing) at all considered wavelengths.

3.1.1. Clouds & hazes profiles

We consider a simplified version of the bimodal distribution derived by Luginin *et al.* (2016). Size distributions and optical properties of both modes are detailed hereafter (§3.3).

Particle number density (in units of particles $\cdot\mathrm{m}^{-3}$) for mode 2 is given by: $n_2(z) = 10^8$ for $z < Z_2$ and $n_2(z) = 10^8 \times \exp\left(\frac{Z_2 - z}{4.5\ \mathrm{km}}\right)$ for $z > Z_2$. The control altitude Z_2 is a fitted parameter. It is related, but should not be confused with the $Z\left(\tau_\lambda = 1\right)$ altitude which classically defines the cloud top altitude (nadir optical depth equal to 1) – e.g. at $\lambda = 250$ nm, we have $Z(\tau = 1) = Z_2 + 4.95$ km.

Particle number density for mode 1 is tied to mode 2 number density profile according to: $n_1(z) = \min\left[2 \times 10^8; 500 \times n_2(z)\right]$.

3.1.2. Gaseous species profiles

The number densities of gas molecules $n_0(z)$ in each layer is computed according to hydrostatic equilibrium, taking into account the decrease of

gravity with increasing altitude (the acceleration of gravity at the bottom of the model being set to 8.725 m/s^2). The temperature profile is taken from VIRA-2 (Moroz and Zasova, 1997), and the molecular mass vertically uniform at 43.4 g/mol. CO_2 and N_2 volume mixing ratios are also vertically uniform – the part of the atmosphere that we model lies entirely within the homosphere – and respectively equal to 96.5% and 3.5%. Adopting a fixed temperature profile is a reasonable approximation, since it has far less consequences for modeling Venus UV reflectivity than for thermal infrared sounding. SO_2 mixing vertical profile is parameterized as follows: $f(z) = \min\left[150 \text{ ppmv}; f_{70\text{ km}} \times \exp\left(\frac{70\text{ km}-z}{3\text{ km}}\right)\right]$. SO_2 mixing ratio at 70 km, $f_{70\text{ km}}$, is the fitted quantity for SO_2.

SO vertical profile follows a simplified parameterization from Krasnopolsky (2018): it is tied to 10% of SO_2 profile from the top of our model downwards, following the same scale height as SO_2 (namely 3 km), reaching a maximum in the lower atmosphere at 1 ppmv, and dropping to 0 below this maximum. Based on our numerical modeling with the Venus LMD-IPSL-GCM (see §4.2), O_3 mixing ratio profile is considered uniform in the 55-70 km range, and null out of this range. Its mixing ratio in the 55-70 km range is a fitted parameter, but we should keep in mind that retrieved O_3 VMR is strongly dependent on our assumed vertical profile. OCS absorption was shown by Haus *et al.* (2015) to be noticeable near 240 nm, so we included (but did not fit) a fixed OCS vertical profile according to the above reference (Haus *et al.*, 2015): $f_{\text{OCS}}(z) = min\left[42.5 \text{ ppbv}; 10^{-7} \times \exp\left(\frac{50\text{ km}-z}{14.427\text{ km}}\right)\right]$.

3.2. Gaseous cross-sections

Absorption cross-sections of CO_2, O_3, OCS, SO_2 and SO are taken from various sources. For CO_2, whose cross-sections were extracted from Parkinson (2003), we interpolated between 195 and 295 K assuming that $\log \sigma_{\rm abs}$ is a linear function of $1/T$. We used the same temperature interpolation for SO_2 cross-sections and used the same primary sources, spectral ranges and temperature range as Jessup *et al.* (2015), namely: (a) Rufus *et al.* (2003) at 295 K and 198 K, above 200 nm; (b) Freeman *et al.* (1984) at 213 K below 240 nm; (c) Wu *et al.* (2000) at 295 K above 240 nm.

Recent SO cross-section measurements are rare in the databases; we used data from Phillips (1981) in the 190-230 nm range provided by Frank Mills (priv. comm.), and extrapolated the cross-section for shorter wavelengths with a best-fitting parabola: $\log_{10}(\sigma_{\rm abs}/{\rm cm}^2) = -\left(\frac{\lambda - 200.132\ {\rm nm}}{20.961\ {\rm nm}}\right)^2 - 16.780$. For wavelengths longer than 230 nm, SO cross-section is taken constant at 3×10^{-20} cm^2.

O_3 cross-section is taken from Sander *et al.* (2011) for a temperature of 218 K in the 196-343 nm range. OCS cross-section is also taken from Sander *et al.* (2011) for a temperature of 225 K in the 186-292 nm range.

CO_2, SO_2 and SO absorption cross-sections feature a line-resolving, high spectral resolution (around 0.2 nm). Our forward model is however used here at a coarser spectral resolution (since SPICAV-UV FWHM is around 1 nm) through the convolution within a Gaussian window of the computed high-resolution transmission in each computational layer, which is then converted to a low-resolution optical depth: $\tau = -\ln[\langle T \rangle]$ where T is the transmission and $\langle\rangle$ stands for the running average of the spectral transmission over the

chosen spectral resolution. Rayleigh scattering cross sections for CO_2 and N_2 are taken from Sneep and Ubachs (2005).

3.3. Mie theory calculations

The radiative transfer model requires the scattering properties of both mode 1 and mode 2 that make up the clouds and haze of Venus. These properties are: their single scattering albedo $\varpi_0(\lambda)$, the extinction cross-section $\sigma_{\text{ext}}(\lambda)$, the coefficients of the Legendre expansion of their phase functions $p_i(\lambda)$. They are computed using the standard `BHMIE` Fortran implementation of the Bohren and Huffman (1983) code for 17 discrete wavelengths from 170 to 320 nm every 10 nm. A bimodal particle distribution is considered, assuming a log-normal distribution following Luginin *et al.* (2016): $r_{\text{eff}} = 0.12$ µm, $\nu_{\text{eff}} = 0.15$ for mode 1; $r_{\text{eff}} = 0.8$ µm, $\nu_{\text{eff}} = 0.15$ for mode 2. The real part of the refractive index follows $m_r(\lambda) = 1.526 - 3.05 \times 10^{-4}\,(\lambda - 200\text{ nm})$ according to Hummel *et al.* (1988) for a $75\% - 25\%$ H_2SO_4-H_2O mixture. The imaginary part of the refractive index is assumed to be $m_i(\lambda) = 10^{-3}$ for mode 2 particles, and $m_i(\lambda) = m_i(250\text{ nm}) \times \exp\left(\frac{\lambda - 250\text{ nm}}{50\text{ nm}}\right)$ for mode 1 particles. $m_i(250\,\text{nm})$ is an adjustable parameter representative of the unknown UV absorber concentration in mode 1 droplets. Both these choices for m_i allow our retrievals for cloud top altitudes and m_i to be consistent with commonly accepted values (Ignatiev *et al.*, 2009; Titov, 2017), as well as minimizing spurious correlations of our cloud parameters with airmass and/or solar zenith angle. Please note that SO_2 and O_3 retrievals, which exhibit a specific spectral dependency (absorption bands), do not suffer from this degeneracy. Look-up tables of mode 1 and mode 2 optical properties are computed every 10 nm from 170 to 320 nm, and for 11 values of $m_i(250\text{ nm})$

ranging from 10^{-4} to 2×10^{-1}.

3.4. Fitting strategy

3.4.1. Choice of fitted parameters

Since SPICAV did not allow for resolving the individual gaseous spectral lines, we are usually able to fit three parameters in our observed spectra in order to account for the three distinctive features in those spectra, namely (a) their spectral average radiance factor; (b) a 215 nm-centered absorption band caused by SO and SO_2; (c) a 280 nm-centered absorption band caused by SO_2 alone. Since we cannot distinguish between SO and SO_2 absorption at SPICAV spectral resolution, we chose the following other three parameters to be fitted: (a) SO_2 abundance at 70 km; (b) cloud top altitude at 250 nm, through the Z_2 control point; and (c) imaginary index of mode 1 particles at 250 nm. This choice enables a proper fitting of both absorption bands, since altering Z_2 changes the relative weight of both absorption bands due to the the difference in Rayleigh scattering by CO_2 as well as difference in single scattering albedo of mode 1 particles between 215 and 280 nm.

Also, following Frandsen *et al.* (2016), we also considered the possibility of UV contrasts being caused by OSSO, by implementing their analytical cross-section for both cis- and trans-isomers of OSSO, as well as their calculated vertical profile. However, we could not obtain satisfactory fits of the observed radiance factors in this way, OSSO absorption having a negligible influence over the modeled radiance factor unless unrealistically high abundances (peaking well over 1 ppmv at 62 km) were prescribed, which in this case resulted in the suppression of other spectral features. Following Krasnopolsky (2018), we therefore claim that the OSSO profile computed

by Frandsen *et al.* (2016) cannot account for the UV radiance observed by SPICAV-UV.

A fourth parameter, absorption depth near 250 nm caused by ozone, can be measured on a sizable minority of the spectra as extensively discussed in §3.4.2. The analysis of the results obtained for the other fitted quantities will be discussed in another paper.

3.4.2. Criterion for O_3 detection

The fact that we do have systematic errors that account significantly for our reduced χ^2 values (median value at 28.6 without O_3) prevents us from using a simple difference criterion between χ^2 without considering O_3 and χ'^2 when introducing O_3 as an extra degree of freedom. So we decided to use the more robust *improvement ratio* $r = \chi^2/\chi'^2$ instead.

Some observed radiance factors show indeed a distinctive improvement of their reduced χ^2 once O_3 is allowed to vary in the forward model (Fig. 3): for these spectra, it is impossible to reach a satisfactory agreement between observations (high radiance in the 210-230 nm range, concavity near 250 nm) and our forward model without adding O_3 absorption near 250 nm, allowing at the same time for a lower SO_2 and SO absorption. Therefore, in order to distinguish between genuine and spurious detections of O_3, we investigated the improvement ratio for all spectra. The results are shown in Fig. 4. Most spectra actually benefit little from the inclusion of O_3, with a marginal increase of r less than 1.5. However, a sizable minority of spectra, especially at latitudes higher than 50°, display r well in excess of 5. In order to avoid false positives (at the expense of discarding some actual detections), we decided to trust our O_3 measurements only if $r > 5.5$, corresponding to a p-value of

0.27% (3-σ) assuming that the quantity $-2(r-1)$ (which is reminiscent of a likelihood ratio test statistics) follows a χ^2 law with one degree of freedom (corresponding to the additional one parameter, namely O_3 VMR) according to Wilk's theorem. Incidentally, a similar value for r was also considered by Montmessin *et al.* (2011) in their SPICAV-UV occultation detection of O_3.

3.4.3. Probed altitude range

Spectroscopic measurements of minor species using backscattered solar light are sensitive to *column densities* instead of absolute mixing ratios. Therefore, in order to convert our fitted O_3 mixing ratios into column densities and compare them with values obtained on Earth or Mars (Perrier *et al.*, 2006), we need to know the penetration depth of backscattered photons. Monte-Carlo radiative transfer modeling would readily yield such a quantity, but discrete ordinate radiative transfer solvers (like DISORT) do not. In order to derive this quantity, we designed the following algorithm:

1. For a given model atmosphere and wavelength, run our forward model and store the modeled radiance factor R_0;
2. Replace a given computational layer located at altitude z with an optically thick and absorbing layer. The resulting radiance factor $R(z)$ will be $0 < R(z) < R_0$, with $R(z) \to 0$ as z increases towards the observer, and $R(z) \to R_0$ for a deep layer that backscattered photons do not usually reach;
3. Locate the altitude z_1 where $R(z_1)/R_0 = 1/2$. This altitude z_1 defines our effective scattering altitude.

Figure 3: Best fits obtained considering (solid orange) and discarding (solid blue) O_3. An O_3-rich observation is shown on upper left planel, marginal O_3 detection in the upper right panel and a non-detection of O_3 on the lower left panel, according to our improvement ratio criterion. Gaseous cross-sections taken into account in our model are shown on the lower right panel.

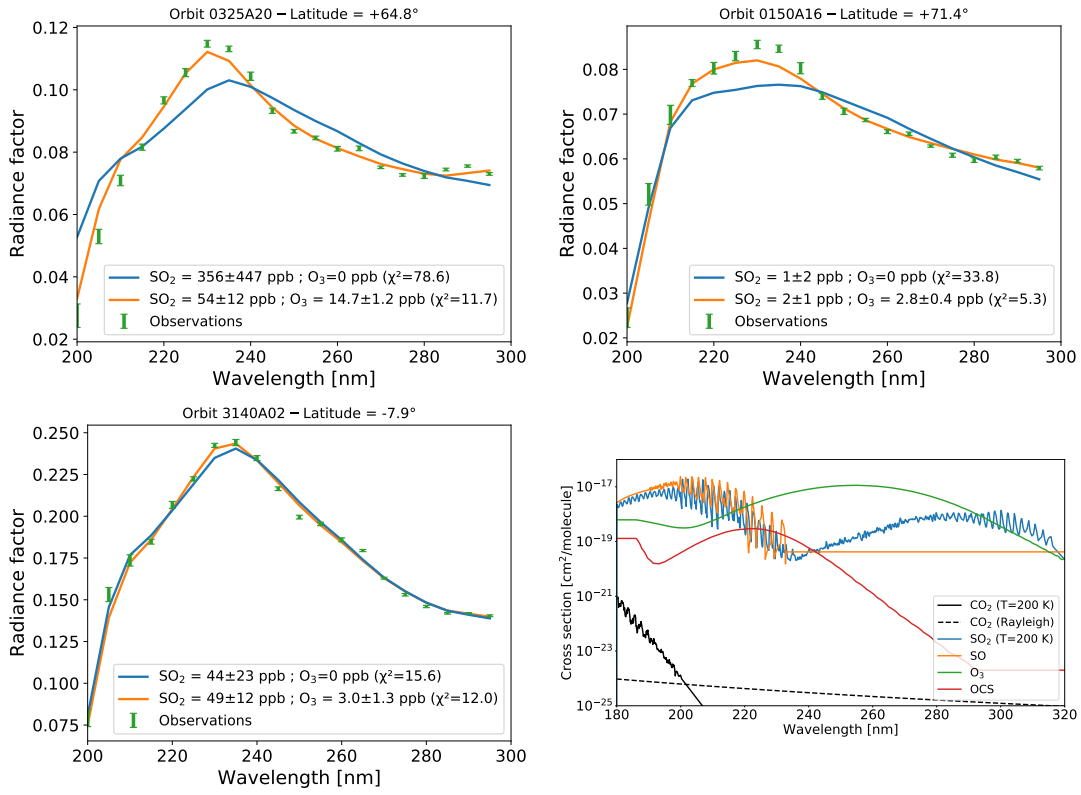

Figure 4: Density plot of χ^2 improvement ratio (without O_3/with O_3) according to latitude. The adopted threshold (5.5) is shown in solid red.

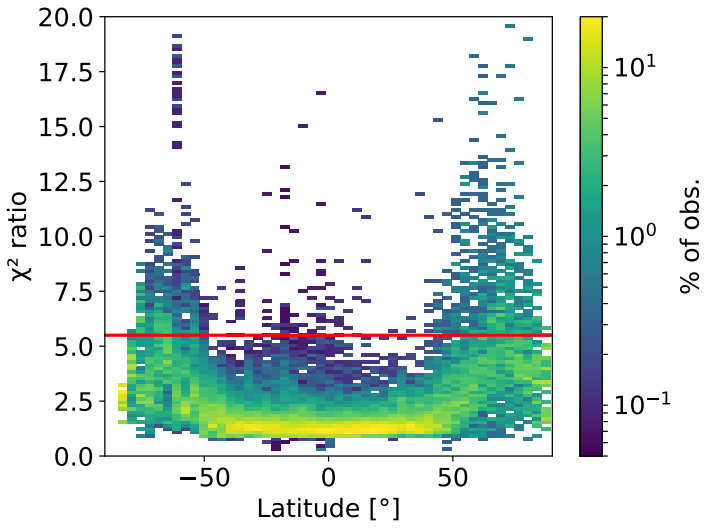

This algorithm may even be extended to derive the "optical stiffness" of the atmosphere: assuming a normal distribution for the backscattering altitude, we can compute its 1-standard deviation interval, using respectively 0.5 ± 0.341 as values for $R(z)/R_0$. The resulting effective scattering altitude distribution is shown in Fig. 5. Shorter wavelengths probe higher in Venus atmosphere, which is expected considering that they are on the edge of a strong CO_2 absorption band. For wavelengths longer than 240 nm, the effective scattering altitude is uniform within ± 2 km, whereas the standard deviation of scattering altitudes is on the order of ± 5 km, close to the atmospheric scale height. We will therefore consider that our model probed the two scale heights below the cloud top level ($\tau = 1$ at 250 nm is located at an altitude of 74 km for the computations shown in Fig. 5). Incidentally,

Figure 5: Effective scattering altitude for our typical model atmosphere (solid orange) and $\pm 1\sigma$ deviation (dashed orange).

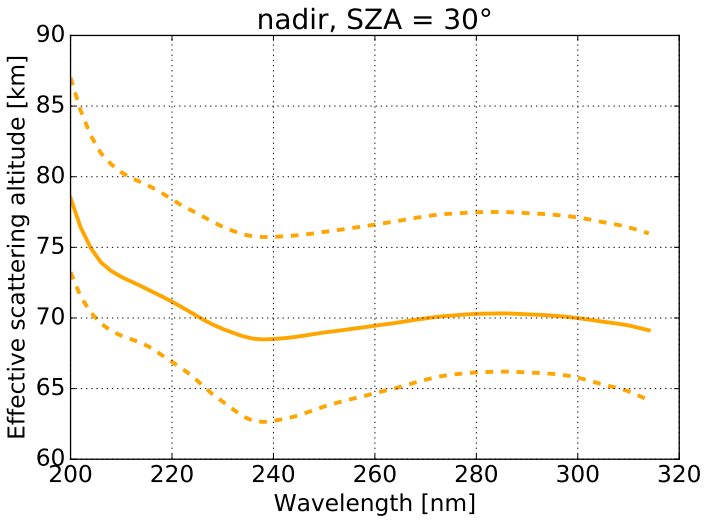

Figure 5 also confirms that the two SO_2 bands centered near 215 and 280 nm do not probe exactly at the same altitude, with the 215 nm band probing about 2 km higher on average.

4. Results

4.1. Observed Ozone distribution

First of all, as could already be seen on Fig. 4, Fig. 6 shows that the overwhelming majority of O_3 detections took place polewards of 50°. The detection threshold is around 2-3 ppbv in the probed altitude range. The typical maximal mixing ratio in both hemispheres lies in the 10-20 ppbv range considering our assumed vertical profile between 55 and 70 km in altitude, the location of the maximum in the northern polar region being $80°N$, in the cold

collar region. Retrievals in the southern hemisphere are less numerous (6.7% of positive detections polewards of 50°S compared with 18.2% of positive detections polewards of 50°N), which is expected since the quasi-polar orbit of *Venus Express* with a pericenter near 78°N made nadir observations of the northern hemisphere easier and more accurate. Keeping this fact in mind, mixing ratios in the southern hemisphere (median and $\pm 1\sigma$ dispersion of $11.4^{+4.2}_{-3.3}$ ppbv) look comparable to those found in the northern hemisphere (median and $\pm 1\sigma$ dispersion of $9.4^{+4.3}_{-3.7}$ ppbv), albeit somewhat higher and without any evidence for a symmetrical peak near 80°S. Detections at lower latitudes are most likely spurious and not significant – about 0.55%, which is close to the expected false positive rate considering our retained 0.27% p-value threshold discussed in §3.4.2. The fact that this cloud top O_3 only exists at high latitudes may explain why it eluded detection until now, since these latitudes are barely observable from Earth due to Venus small axial tilt with respect to the ecliptic.

Translated in column densities between 65-70 km (since most backscattered photons have not ventured below 65 km, see §3.4.3), these maximal mixing ratios are in the 0.1-0.5 DU range. This is comparable to typical values on Mars out of the dry polar vortices, although one order of magnitude less than the maximal values on Mars in the dry polar vortices – typically 4-5 DU according to Perrier *et al.* (2006). It is also three orders of magnitude less than our Earth's ozone layer – typically 300 DU, which corresponds to a layer of 3 mm thickness of pure ozone under STP conditions ($1\ \mathrm{DU} \approx 2.69 \cdot 10^{16}\ O_3\ \mathrm{molecules/cm^2}$).

Figure 6 may hint at some level of local solar time (LST) variability,

Figure 6: Latitudinal plot of O_3 mixing ratio with respect to latitude. Color codes for local solar time. Solid red lines and error bars stand for running average and statistical dispersions within 5°-wide latitudinal bins.

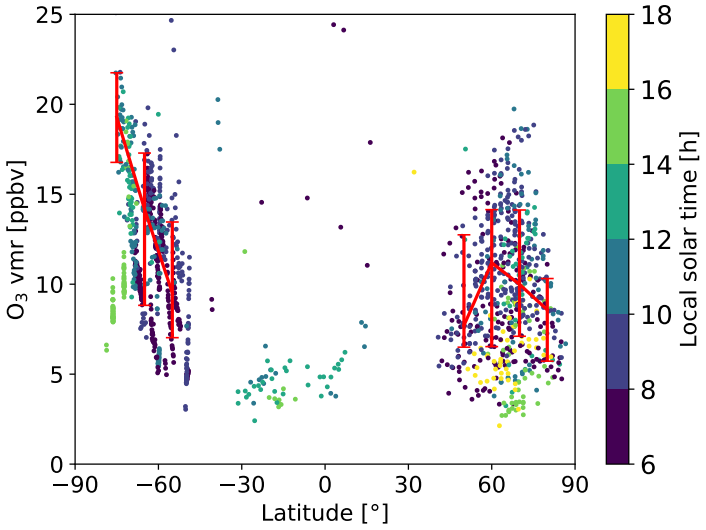

at least for higher quality measurements in the northern hemisphere, with more O_3 near the morning terminator than near the evening. However, we must keep in mind that, unlike the daily latitudinal sweeping resulting from the polar orbit, the observed local time only varied slowly, along with the precession of *Venus Express* orbit with respect to sub-spacecraft local solar time. So that it is difficult from our data alone to disentangle local time variability from possible long-term, secular variations. Since no such local time asymmetry is visible for the southern hemisphere measurements in Fig. 6, a weak secular trend is indeed a more likely explanation. Our average maps in Fig. 7 confirm this ambiguity: a morning/evening asymmetry is likely in the northern hemisphere, but alternatively, there could be a slight secular increase of O_3 during the whole *Venus Express* mission. Whether this secular O_3 increase, if genuine, is linked to the known secular variations of cloud top SO_2 (Esposito *et al.*, 1988; Marcq *et al.*, 2013) is a question of interest for future observers and photochemical modelers.

4.2. Comparison with general circulation model with photochemistry

The existence of a polar ozone layer at the Venus cloud top is theoretically predicted by the LMD IPSL general circulation model (GCM) from Lebonnois *et al.* (2010). In its version with coupled photochemistry (Stolzenbach *et al.*, 2014), the LMD model shows the formation of a distinct ozone maximum between 55-65 km in both hemispheres poleward of 60° (Fig. 8). Both the altitude and the latitude range of the simulated cloud top ozone layers show a strong similarity with the SPICAV observations, at least from a qualitative point of view.

As already diagnosed in the LMD GCM simulations of Lebonnois *et al.*

Figure 7: *Left:* median map of cloud top O_3 with respect to latitude and LST. *Right:* median pseudo-map of cloud top O_3 with respect to latitude and date of observation

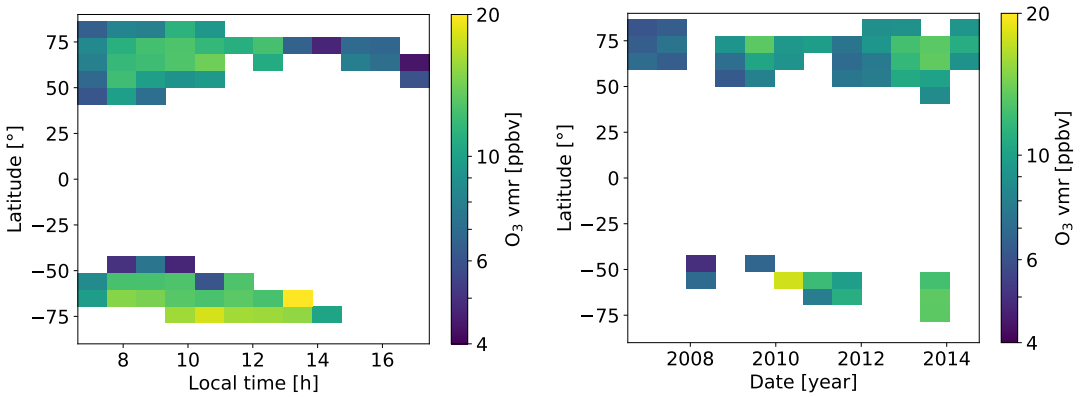

(2010), the Venus mean meridional circulation is organized in large-scale Hadley cells throughout the upper cloud and mesosphere. In this type of circulation, subsiding motion occurs permanently over both polar regions and transports chemical species downwards from the upper atmosphere to lower altitudes. Obviously this process mostly impacts the distribution of long-lived species, which are little affected by chemical processes and quasi-conserved during their slow downward transport towards the poles. Figure 8 illustrates the effect of the Hadley circulation on O and O_2. Both species are essentially produced in the upper atmosphere and are the source species of ozone through the reaction :

$$O + O_2 + CO_2 \longrightarrow O_3 + CO_2 \tag{1}$$

Figure 8 shows that the mean meridional circulation has little effect on the O distribution below 95 km, owing to the short photochemical lifetime

Figure 8: Zonally averaged mixing ratio (ppbv) of O_3 (above), O (lower left) and O_2 (lower right) calculated by the LMD general circulation model.

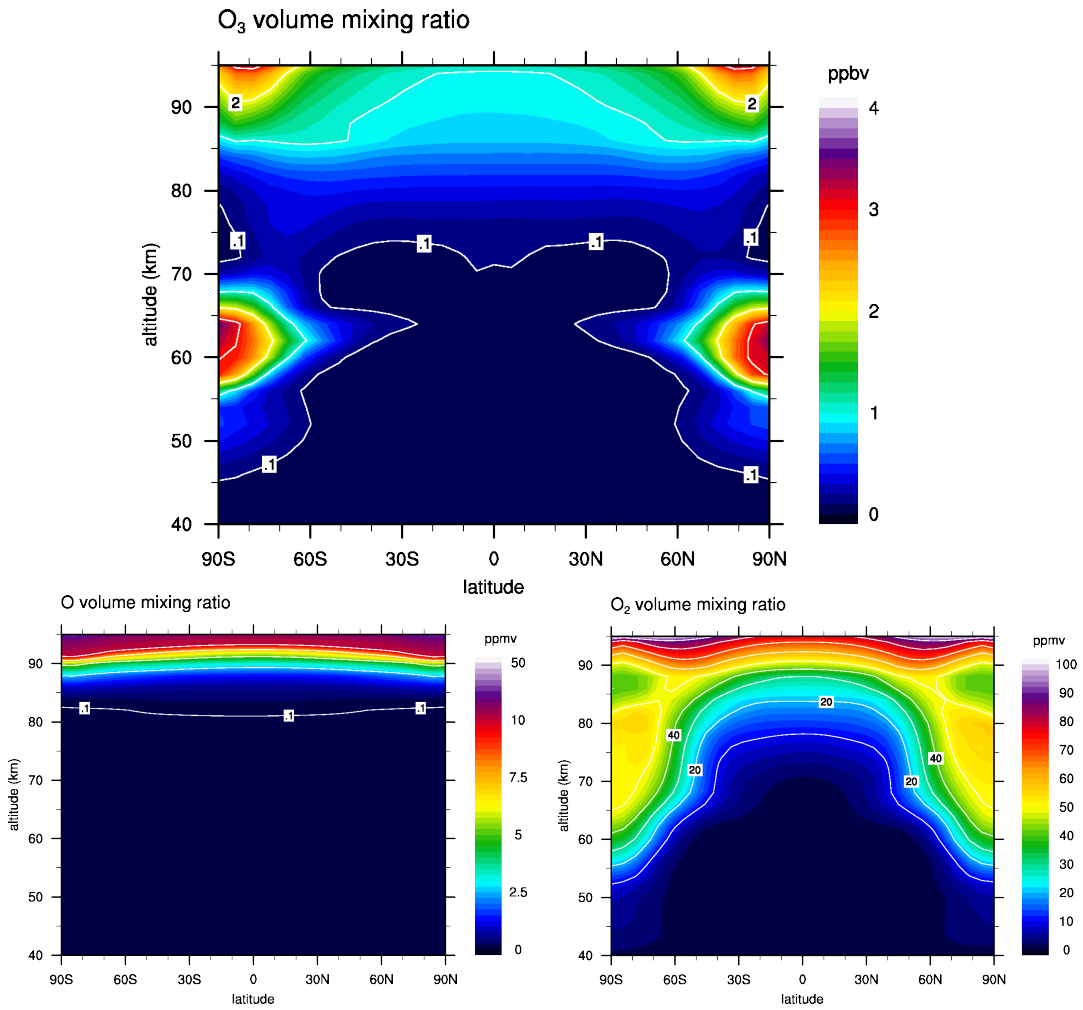

(minutes) of O atoms in this altitude range. In contrast, with a lifetime of several years, O_2 is dramatically impacted by the Hadley circulation. Downward transport of upper atmosphere O_2 increases its mixing ratio by one order of magnitude over the polar regions. This ultimately leads to the formation of an ozone layer at the cloud top, where the air density becomes sufficiently large to promote the efficiency of the three-body reaction (Eq. 1).

Thus, we argue from the LMD GCM simulation that the cloud top ozone detected by SPICAV is a visible signature of the Hadley meridional circulation on Venus. This process of ozone formation caused by the deep vertical downwelling of oxygen-rich air masses over the pole is similar to that identified on Mars by Montmessin and Lefèvre (2013) using the SPICAM instrument. Nevertheless, despite a good qualitative agreement, on Venus the mean ozone mixing ratio (about 3 ppbv) calculated by the LMD GCM in the polar layer is smaller by a factor of five than the ozone retrieved from SPICAV observations. This suggests that the GCM underestimates the amount of O_2 mixing ratios that are present near the poles at the cloud top. Alternatively, the ozone loss mechanisms by sulfur and chlorine species might be overestimated in the model. We should however note that our retrieved O_3 mixing ratio is very dependent on the assumed vertical profile. In any case, the reasons for this quantitative discrepancy will be investigated in a forthcoming study.

4.3. Comparison with previous O_2 measurements

The observed existence of cloud top O_3 implies that its precursor species O_2 is also present, as can be seen in Fig. 8 above, with a typical high latitude mixing ratio of 50 ppmv near cloud top. These values are well in excess of the

previously known O_2 upper limits (Marcq *et al.*, 2018) of about 2 ppmv above 300 mbar, which are based on near infrared high-resolution spectroscopic observations of Venus day side by Mills (1999) using UHRF/AAT.

We therefore investigated those O_2 upper limit measurements and we found that all of their observations were restricted to latitudes lower than 50° – slit offset of 0.5 to 0.7 Venus radii from the observed disk center according to Mills (1998). At these relatively lower latitudes, the LMD-GCM does not predict any significant O_2 in the 50-70 km altitude range (Fig. 8), nor do we observe any O_3 (Fig. 6). Therefore, we claim that our O_3 discovery remains consistent with known observational limits on its source species O_2. Furthermore, if O_3 – and therefore O_2 – abundances are subject to secular variations, as suggested in Fig. 7 (right), it is also possible that Mills (1999) measurements were performed at a time of relative O_2 scarcity.

5. Conclusion

We have collected robust observational evidence for a newly discovered ozone layer in the upper clouds of Venus, restricted to latitudes higher than 50° in both hemispheres. These findings do not contradict previous observational constraints (restricted to lower latitudes). Due to its dynamical formation mechanism, this ozone layer was not predicted by 1D photochemical models. On the other hand, such a high-latitude ozone layer is predicted by our 3D photochemical model (Stolzenbach *et al.*, 2014), which indicates that this O_3 layer is formed through a mechanism similar to that found in the Martian upper atmosphere (Montmessin and Lefèvre, 2013). The Venus polar ozone layer is however about 10 times thinner than on Mars in terms of

observable column densities (0.1 to 0.5 DU), with no obvious seasonal effect and/or temporal trend in this case.

This discovery also strengthens the argument against using the sole O_3 detection as a proxy for planetary habitability, since even in our own solar system, O_3 is found in the 1 to 10 mbar pressure range in all three telluric atmospheres, although two out of three (Venus and Mars) do not meet the usual criteria for planetary habitability. Actually, in order to protect surface life from harmful stellar UV radiation, one has to find at least ~ 100 DU of ozone in the atmosphere of a planet or exoplanet. In the solar system, only Earth exceeds this value.

Acknowledgements

We wish to acknowledge the support of CNES and ESA for this work. As a result from this support, it is planned to deliver to ESA Planetary Science Archives (PSA) both the day side nadir UV albedo spectra and the columns of SO_2 and ozone derived form SPICAV/Venus Express mission. EM, JLB, FL and FM acknowledge support Tby the Programme National de Planétologie (PNP) of CNRS-INSU co-funded by CNES. DB, OK and JLB wish to acknowledge the support of the Ministry of Education and Science of Russian Federation grant 14.W03.31.0017

Barth, C.A., Hord, C.W., Stewart, A.I., Lane, A.L., Dick, M.L., Anderson, G.P., 1973. Mariner 9 Ultraviolet Spectrometer Experiment: Seasonal Variation of Ozone on Mars. Science 179, 795–796.

Bertaux, J.L., Nevejans, D., Korablev, O., Villard, E., Quémerais, E., Neefs, E., Montmessin, F., Leblanc, F., Dubois, J.P., Dimarellis, E., Hauchecorne,

A., Lefèvre, F., Rannou, P., Chaufray, J.Y., Cabane, M., Cernogora, G., Souchon, G., Semelin, F., Reberac, A., van Ransbeek, E., Berkenbosch, S., Clairquin, R., Muller, C., Forget, F., Hourdin, F., Talagrand, O., Rodin, A., Fedorova, A., Stepanov, A., Vinogradov, I., Kiselev, A., Kalinnikov, Y., Durry, G., Sandel, B., Stern, A., Gérard, J.C., 2007. SPICAV on Venus Express: Three spectrometers to study the global structure and composition of the Venus atmosphere. Plan. and Space Sci. 55, 1673–1700.

Biggs, D.S.C., Andrews, M., 1997. Acceleration of iterative image restoration algorithms. Appl. Opt. 36, 1766–1775.

Bohlin, R.C., Gordon, K.D., Tremblay, P.E., 2014. Techniques and review of absolute flux calibration from the ultraviolet to the mid-infrared. Publications of the Astronomical Society of the Pacific 126, 711.

Bohren, C.F., Huffman, D.R., 1983. Absorption and scattering of light by small particles.

Dahlback, A., Stamnes, K., 1991. A new spherical model for computing the radiation field available for photolysis and heating at twilight. Planet. Space Sci. 39, 671–683.

Esposito, L.W., Copley, M., Eckert, R., Gates, L., Stewart, A.I.F., Worden, H., 1988. Sulfur dioxide at the Venus cloud tops, 1978-1986. J. Geophys. Res. 93, 5267–5276.

Frandsen, B.N., Wennberg, P.O., Kjaergaard, H.G., 2016. Identification of OSSO as a near-UV absorber in the Venusian atmosphere. Geophys. Res. Lett. 43, 11.

Freeman, D.E., Yoshino, K., Esmond, J.R., Parkinson, W.H., 1984. High resolution absorption cross section measurements of SO_2 at 213 K in the wavelength region 172-240 nm. Planet. Space Sci. 32, 1125–1134.

Haus, R., Kappel, D., Arnold, G., 2015. Radiative heating and cooling in the middle and lower atmosphere of Venus and responses to atmospheric and spectroscopic parameter variations. Planet. Space Sci. 117, 262–294.

Hummel, J.R., Shettle, E.P., Longtin, D.R., 1988. A new background stratospheric aerosol model for use in atmospheric radiation models. Technical Report. OPTIMETRICS INC BURLINGTON MA.

Ignatiev, N.I., Titov, D.V., Piccioni, G., Drossart, P., Markiewicz, W.J., Cottini, V., Roatsch, T., Almeida, M., Manoel, N., 2009. Altimetry of the Venus cloud tops from the Venus Express observations. Journal of Geophysical Research (Planets) 114, 0–9.

Jessup, K.L., Marcq, E., Mills, F., Mahieux, A., Limaye, S., Wilson, C., Allen, M., Bertaux, J.L., Markiewicz, W., Roman, T., Vandaele, A.C., Wilquet, V., Yung, Y., 2015. Coordinated Hubble Space Telescope and Venus Express Observations of Venus' upper cloud deck. Icarus 258, 309–336.

Krasnopolsky, V.A., 2013. Nighttime photochemical model and night airglow on Venus. Planet. Space Sci. 85, 78–88.

Krasnopolsky, V.A., 2018. Disulfur dioxide and its near-UV absorption in the photochemical model of Venus atmosphere. Icarus 299, 294–299.

Lebonnois, S., Hourdin, F., Eymet, V., Crespin, A., Fournier, R., Forget, F., 2010. Superrotation of Venus' atmosphere analyzed with a full general circulation model. Journal of Geophysical Research (Planets) 115, E06006.

Luginin, M., Fedorova, A., Belyaev, D., Montmessin, F., Wilquet, V., Korablev, O., Bertaux, J.L., Vandaele, A.C., 2016. Aerosol properties in the upper haze of Venus from SPICAV IR data. Icarus 277, 154–170.

Marcq, E., Belyaev, D., Montmessin, F., Fedorova, A., Bertaux, J.L., Vandaele, A.C., Neefs, E., 2011. An investigation of the SO_2 content of the venusian mesosphere using SPICAV-UV in nadir mode. Icarus 211, 58–69.

Marcq, E., Bertaux, J.L., Montmessin, F., Belyaev, D., 2013. Variations of sulphur dioxide at the cloud top of Venus's dynamic atmosphere. Nature Geoscience 6, 25–28.

Marcq, E., Mills, F.P., Parkinson, C.D., Vandaele, A.C., 2018. Composition and Chemistry of the Neutral Atmosphere of Venus. Space Sci. Rev. 214, #10.

McClintock, W.E., Rottman, G.J., Woods, T.N., 2005. Solar-Stellar Irradiance Comparison Experiment II (SOLSTICE II): Instrument Concept and Design. Springer New York, New York, NY. pp. 225–258.

Mills, F.P., 1998. I. Observations and Photochemical Modeling of the Venus Middle Atmosphere. I. Thermal Infrared Spectroscopy of Europa and Callisto. Ph.D. thesis. CALIFORNIA INSTITUTE OF TECHNOLOGY.

Mills, F.P., 1999. A spectroscopic search for molecular oxygen in the Venus middle atmosphere. J. Geophys. Res. 104, 30757–30764.

Montmessin, F., Bertaux, J.L., Lefèvre, F., Marcq, E., Belyaev, D., Gérard, J.C., Korablev, O., Fedorova, A., Sarago, V., Vandaele, A.C., 2011. A layer of ozone detected in the nightside upper atmosphere of Venus. Icarus 216, 82–85.

Montmessin, F., Lefèvre, F., 2013. Transport-driven formation of a polar ozone layer on Mars. Nature Geoscience 6, 930–933.

Moroz, V.I., Zasova, L.V., 1997. VIRA-2: a review of inputs for updating the Venus International Re ference Atmosphere. Advances in Space Research 19, 1191–1201.

Parkinson, W., 2003. Absolute absorption cross section measurements of CO_2 in the wavelength region 163-200 nm and the temperature dependence. Chemical Physics 290, 251–256.

Perrier, S., Bertaux, J.L., Lefèvre, F., Lebonnois, S., Korablev, O., Fedorova, A., Montmessin, F., 2006. Global distribution of total ozone on Mars from SPICAM/MEX UV measurements. Journal of Geophysical Research (Planets) 111, E09S06.

Phillips, L.F., 1981. Absolute absorption cross sections for SO between 190 and 235 nm. Journal of Physical Chemistry 85, 3994–4000.

Rufus, J., Stark, G., Smith, P.L., Pickering, J.C., Thorne, A.P., 2003. High-resolution photoabsorption cross section measurements of SO_2, 2: 220 to 325 nm at 295 K. Journal of Geophysical Research (Planets) 108, 5011–5016.

549 Sander, S.P., Abbatt, J., Barker, J.R., Burkholder, J.B., Friedl, R.R.,
550 Golden, D.M., Huie, R.E., Kolb, C.E., Kurylo, M.J., Moortgat, G.K.,
551 Orkin, V.L., Wine, P.H., 2011. Chemical Kinetics and Photochemical
552 Data for Use in Atmospheric Studies, Evaluation number 17. Technical
553 Report. Jet Propulsion Laboratory.

554 Sneep, M., Ubachs, W., 2005. Direct measurement of the Rayleigh scattering
555 cross section in various gases. Journal of Quantitative Spectroscopy and
556 Radiative Transfer 92, 293–310.

557 Stamnes, K., Tsay, S., Jayaweera, K., Wiscombe, W., 1988. Numerically
558 stable algorithm for discrete-ordinate-method radiative transfer in multiple
559 scattering and emitting layered media. Appl. Opt. 27, 2502–2509.

560 Stolzenbach, A., Lefèvre, F., Lebonnois, S., Määttänen, A., Bekki, S., 2014.
561 Three-dimensional modelling of Venus photochemistry, in: EGU General
562 Assembly Conference Abstracts, p. 5315.

563 Titov, D., 2017. Venus book cloud chapter. Space Sci. Rev. .

564 White, R.L., 1994. Image restoration using the damped richardson-lucy
565 method.

566 Wu, R.C.Y., Yang, B.W., Chen, F.Z., Judge, D.L., Caldwell, J., Trafton,
567 L.M., 2000. Measurements of High-, Room-, and Low-Temperature Pho-
568 toabsorption Cross Sections of SO_2 in the 2080- to 2950-Å Region, with
569 Application to Io. Icarus 145, 289–296.

570 Yung, Y.L., Demore, W.B., 1982. Photochemistry of the stratosphere of
571 Venus - Implications for atmospheric evolution. Icarus 51, 199–247.